Identifying the linear phase of the relativistic Kelvin-Helmholtz instability and measuring its growth rate via radiation

R. Pausch, M. Bussmann, A. Huebl, U. Schramm, K. Steiniger, R. Widera, and A. Debus

Phys. Rev. E **96**, 013316 — Published 26 July 2017

DOI: 10.1103/PhysRevE.96.013316

Identifying the linear phase of the relativistic Kelvin-Helmholtz instability and measuring its growth rate via radiation

R. Pausch,[1,2] M. Bussmann,[1] A. Huebl,[1,2] K. Steiniger,[1,2] R. Widera,[1] and A. Debus[1]

[1] *Helmholtz-Zentrum Dresden - Rossendorf, Bautzner Landstraße 400, 01328 Dresden, Germany*
[2] *Technische Universität Dresden, 01062 Dresden, Germany*

(Dated: April 4, 2017)

For the relativistic Kelvin-Helmholtz instability (KHI) which occurs at shear interfaces between two plasma streams, we report results on the polarized radiation over all observation directions and frequencies emitted by the plasma electrons from ab-initio kinetic simulations. We find the polarization of the radiation to provide a clear signature for distinguishing the linear phase of the KHI from its other phases. During the linear phase, we predict the growth rate of the KHI radiation power to match the growth rate of the KHI to a high degree. Our predictions are based on a model of the vortex dynamics which describes the electron motion in the vicinity of the shear interface between the two streams. Albeit the complex and turbulent dynamics happening in the shear region, we find excellent agreement between our model and large-scale particle-in-cell simulations. Our findings pave the way for identifying the KHI linear regime and for measuring its growth rate in astrophysical jets observable on earth as well as in laboratory plasmas.

I. INTRODUCTION

The relativistic Kelvin-Helmholtz instability (KHI) is a fundamental plasma instability that occurs due to shearing at the boundary between two plasma streams of relativistic relative speed. In the so-called linear phase [1] of the KHI, magnetic fields at this boundary grow exponentially in strength and turbulent vortices appear in the plasma. The KHI is central to understanding strong magnetic field generation, particle acceleration and X-ray radiation in astrophysical jets [2–6] and plays an important role in inertial confinement fusion and accelerator physics [7, 8]. Recent theoretical studies [1, 9–12] were able to show the emergence of large-scale DC magnetic fields at the shear interface by applying kinetic instead of hydrodynamic methods. However, comparisons to observations were so far limited, since observational data does not directly probe plasma dynamics, but derives its results from electro-magnetic radiation [13].

In this work, we report for the first time on a distinct radiation signature of the KHI and link it to the microscopic plasma dynamics in the shear region. We present results of the largest, most detailed particle-in-cell simulation [14] of the relativistic KHI, covering a 46 times larger volume at 4.2 times higher spatial resolution than in any previous simulation [15]. In contrast to previous radiation simulations [13, 16–26], time-resolved polarized radiation emitted by electrons is calculated in-situ based on Liénard-Wiechert potentials [27, 28] taking into account 19 billion particle trajectories, thus tracing every second electron in the simulation. We develop a kinetic model of the KHI vortex dynamics that predicts the polarization components of the radiation emitted to take on characteristic values. This allows for unambiguous identification of the linear phase, independent of a specific observer's inertial frame of reference. Our model further shows that the growth rate Γ_{rad} of the total radiation power during this phase equals the growth rate Γ_{Bz} of the magnetic field energy in the KHI. With this prediction a measurement of the KHI growth rate in astrophysical scenarios via the radiation growth rate becomes possible and will provide strong constraints on central properties of distant jets [29] such as density, velocity gradients and species composition of the plasma streams.

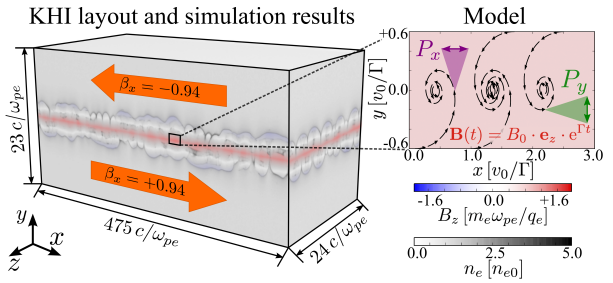

Figure 1. (Left) illustration of the Kelvin-Helmholtz instability (KHI) in the relative velocity frame with two counter-propagating plasma streams, showing the magnetic field strength and electron density from the simulation [14] at $t = 31\omega_{pe}^{-1}$. (Right) illustrates vortex trajectories based on a microscopic model [Eq. (2)] and the emitted radiation with its characteristic polarization P_x and P_y.

II. MODELING THE KHI LINEAR PHASE

The KHI is usually found in scenarios where a plasma jet shears against the surrounding interstellar medium [30]. We model this in a relative velocity frame where plasma streams have the same absolute speed but propagate in opposite directions [14] [Fig. 1] which has the advantage of being numerically more stable to simulate. The initial drift and Maxwellian velocity distribution of charged plasma particles seeds a magnetic field B_z at the shear interface between both streams. This field acts back on the plasma and starts growing exponentially due to a self-amplifying feedback mechanism. In

this regime, named the *linear phase*, the magnetic field dominates the electron dynamics and creates characteristic electron vortices [10].

For the sake of simplicity, our kinetic model assumes that only the strongest field component B_z governs the electron dynamics during the linear phase of the KHI, even though all magnetic field components grow exponentially [15]. This is reasonable since the other magnetic field components are at least one order of magnitude weaker than B_z [15]. Apart from this dominant magnetic field acting on the electrons we consider no additional forces that might arise from electric fields or collisions. We thus assume a spatially homogeneous magnetic field

$$\boldsymbol{B}(t) = B_0 \cdot \boldsymbol{e}_z \cdot e^{\Gamma t}\,, \tag{1}$$

inside the small volume comprising the shear interface [Fig. 1], with B_0 denoting the initial magnetic field value and Γ the exponential growth rate of the KHI.

Via the Lorentz force, this field [Eq. (1)] acts on all electrons within this volume and accelerates them according to $\ddot{\boldsymbol{r}} = \chi \cdot e^{\Gamma t} \cdot \dot{\boldsymbol{r}} \times \boldsymbol{e}_z$ with $\chi = \frac{q_e \cdot B_0}{\gamma_e \cdot m_e}$ and $\boldsymbol{r}$, q_e, m_e and γ_e being the position, charge, mass and Lorentz factor of the electron. If the initial velocity of an electron is directed in the respective stream direction $\boldsymbol{v}(t=0) = \pm v_0 \cdot \boldsymbol{e}_x$, the solution to the equation of motion becomes

$$\dot{r} = \dot{x} + \mathrm{i}\dot{y} = \pm v_0 \cdot \exp\left(\mathrm{i}\frac{\chi}{\Gamma} \cdot \left(1 - e^{\Gamma t}\right)\right). \tag{2}$$

Integrating Eq. (2) over time leads to an electron trajectory spiraling in the x-y-plane towards a center point as depicted in Fig. 1.

III. DERIVING THE EMITTED RADIATION SIGNATURE

A. Computing far field radiation

In the model, and later in the particle-in-cell simulation, we compute the electromagnetic radiation in the far field approximation by applying Liénard-Wiechert potentials [31]. The spectrally and angularly resolved intensities are obtained by integrating the trajectories of a finite number of N_e electrons[1] over time.

$$\frac{\mathrm{d}^2 I}{\mathrm{d}\,\omega\,\mathrm{d}\,\Omega}(\boldsymbol{n}, \omega, \boldsymbol{F}) = \frac{q_e^2}{16\pi^2 \varepsilon_0 c} \cdot \left| \int_{-\infty}^{+\infty} \sum_{i=1}^{N_e} \boldsymbol{F} \cdot \frac{\boldsymbol{n} \times \left[(\boldsymbol{n} - \boldsymbol{\beta}_i) \times \dot{\boldsymbol{\beta}}_i\right]}{\left(1 - \boldsymbol{n} \cdot \boldsymbol{\beta}_i\right)^2} \cdot \mathrm{e}^{\mathrm{i}\,\omega(t - \boldsymbol{n} \cdot \boldsymbol{r}_i / c)}\,\mathrm{dt} \right|^2 . \tag{3}$$

[1] The selection of these N_e electrons is discussed later in the text.

Here we denote position, speed and acceleration of the i^{th} of all N_e electrons by $\boldsymbol{r}_i$, $\boldsymbol{\beta}_i$ and $\dot{\boldsymbol{\beta}}_i$ while $\boldsymbol{n}$ is the observation direction and ω the emitted frequency. Additionally, we introduce a polarization filter $\boldsymbol{F}$. For $\boldsymbol{F} = \mathbb{1}$ the total radiation is calculated, while setting the filter to a base vector $\boldsymbol{F} = \boldsymbol{e}_{\{x,y,z\}}$ returns the emitted intensity for a polarization parallel to $\boldsymbol{F}$. The degree of polarization of a component j is defined by

$$\langle\, P_j \,\rangle = \frac{\langle\, \epsilon_{\text{rad}}(\boldsymbol{F} = \boldsymbol{e}_j) \,\rangle}{\langle\, \epsilon_{\text{rad}}(\boldsymbol{F} = \mathbb{1}) \,\rangle}, j \in \{x, y, z\} \tag{4}$$

with $\langle\, \epsilon_{\text{rad}}(\boldsymbol{F}) \,\rangle = \int_0^{4\pi} \mathrm{d}\,\Omega \int_0^{\infty} \mathrm{d}\,\omega \frac{\mathrm{d}^2 I}{\mathrm{d}\,\omega\,\mathrm{d}\,\Omega}(\boldsymbol{n}, \omega, \boldsymbol{F})$ being the total radiated energy behind a polarization filter $\boldsymbol{F}$.

B. Polarization signature

Numerically integrating Eq. (4) for spiral trajectories obtained from Eq. (2) yields time-constant parallel $\langle\, \tilde{P}_{\parallel} \,\rangle = \langle\, \tilde{P}_x \,\rangle + \langle\, \tilde{P}_y \,\rangle$ and perpendicular $\langle\, \tilde{P}_{\perp} \,\rangle = \langle\, \tilde{P}_z \,\rangle$ polarizations. Here, the tilde distinguishes model quantities from simulation results. From the model, we obtain the degree of polarization for every component by assuming incoherent radiation and evaluating Eq. (4) for a single arbitrary electron trajectory. In general we expect dominant $P_{\parallel}$ over $P_{\perp}$ as characteristic degree of polarization. The polarization is independent of initial magnetic field B_0 and has only a weak dependence on growth rate Γ and velocity v_0. For our simulation parameters $\Gamma = 0.48\,\omega_{pe}$ and $\gamma = 3$ [14], we calculate $\langle\, \tilde{P}_{\parallel} \,\rangle = 89.8\,\%$ and $\langle\, \tilde{P}_{\perp} \,\rangle = 10.2\,\%$.

C. Correlation between radiation power and KHI growth rate

After identifying the characteristic degree of polarization, we compute the emitted radiation power based on the Larmor equation $\dot{\epsilon}_{\text{rad}} = \frac{\mu_0 q_e^2 \gamma_e^6}{6\pi c}\left[(\dot{\boldsymbol{\beta}})^2 - (\boldsymbol{\beta} \times \dot{\boldsymbol{\beta}})^2\right]$ and the model electron trajectory [Eq. (2)]: $\dot{\tilde{\epsilon}}_{\text{rad}}(t) = \frac{\mu_0 q_e^4 B_0^2 \gamma_e^2}{6\pi c \cdot m_e^2} \cdot \frac{v_0^2}{c^2} \cdot e^{2\Gamma t} \sim e^{2\Gamma t} \equiv e^{\tilde{\Gamma}_{\text{rad}} t}$. This radiation power is the observable of interest for which we have to take into account radiation from both the shear region and the bulk of the KHI, as both contribute to the signal observed on earth. In the simulation we thus sum up all radiation contributions from electrons in the bulk and the interface. Our model, however, is only valid in the shear region and cannot reproduce radiation emitted from other parts of the streams.

As we argue that the radiation signature of the KHI is determined by the electron dynamics, which itself is determined by the magnetic fields, we take all magnetic energy in the simulation volume into account when comparing it to the simulated radiation power. By doing so we will see later in the analysis that the field energy contributions from the bulk are significant at the onset of the

linear phase and thus might overshadow the field energy growth along the shear interface. When comparing model to simulation one thus has to keep in mind over which volume V the corresponding field component B_l, $l \in \{x, y, z\}$, is integrated to calculate the component-wise total magnetic field energy $\epsilon_{Bl}(t) = \int_V \frac{1}{2\mu} B_l^2(\boldsymbol{r}, t)\,\mathrm{d}\,V$. For the model, the integration over a small volume on the shear interface leads to a similar exponential growth $\tilde{\epsilon}_{Bz}(t) = \frac{1}{2\mu} e^{2\Gamma t} \cdot \int B_0^2(\boldsymbol{r})\,\mathrm{d}\,V \sim e^{2\Gamma t} \equiv e^{\tilde{\Gamma}_{Bz} t}$ as the radiation power $\dot{\tilde{\epsilon}}_{\mathrm{rad}}$. Thus, the time derivatives of both the normalized emitted radiation power and the normalized magnetic field energy

$$\frac{\mathrm{d}}{\mathrm{d}\,t} \frac{\dot{\tilde{\epsilon}}_{\mathrm{rad}}(t)}{\dot{\tilde{\epsilon}}_{\mathrm{rad}}(0)} = 2\Gamma\,\mathrm{e}^{2\Gamma t} = \frac{\mathrm{d}}{\mathrm{d}\,t} \frac{\tilde{\epsilon}_{Bz}(t)}{\tilde{\epsilon}_{Bz}(0)} \tag{5}$$

are equal. This equality allows to determine the magnetic field energy growth rate $\Gamma_{Bz} = 2\Gamma$ by measuring the growth rate Γ_{rad} of the emitted radiation power.

IV. VALIDATING THE MODEL BY A 3D PARTICLE-IN-CELL SIMULATION

A. Simulation setup

Since this model is a simplification of realistic KHI scenarios, we assess its range of validity and its ability to discriminate the linear regime and determine its growth rate by comparing it to a large-scale, many-particle simulation. Using two counter-propagating streams of kinetic energy $\gamma_e = 3$, we performed such a simulation [Tab. I] with the relativistic 3D3V particle-in-cell code PIConGPU [14, 32], taking into account the complex relativistic plasma dynamics neglected by the model. The setup is chosen to be an ideal reference setup to clearly isolate the correlation between radiation power and magnetic field evolution. Thus, it uses a step-like velocity gradient, which unambiguously drives the KHI dynamics only. In a more realistic setup, extended velocity gradients or density contrasts will reduce both the magnetic field amplitude at saturation and the growth rate Γ as described in [10]. Following the microscopic model, this will directly reduce the growth rate of the radiation power $\tilde{\Gamma}_{\mathrm{rad}}$, thus allowing measuring the influence of the velocity gradients or density contrasts. The simulated relativistic KHI is in the *mushroom instability* regime [12], but since the radiation depends solely on the orientation of the magnetic field, the same correlation and polarization is expected for the *electron-scale KHI* regime [10]. We computed the radiation [Eq. (3)] [27, 28] emitted by $N_e = 18.9 \times 10^9$ electrons, sampling every second electron in the simulation, resolving both coherent and incoherent radiation for frequencies ranging on a logarithmic scale across 3 orders of magnitudes and covering 481 observation directions on a half-dome solid angle $\Omega = \pi$ [Tab. I]. Due to the large extent of shearing surface and Larmor radii compared to emitted wavelengths, the simulated radiation is predominantly incoherent.

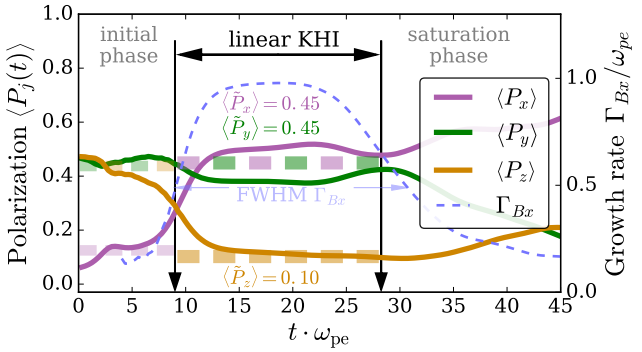

Figure 2. shows the polarization $\langle P_j \rangle$ extracted from simulation, integrated over all observation directions, frequencies and particles [Eq. (4)]. The polarizations expected during the initial phase ($\langle P_y^{\mathrm{syn}} \rangle = \langle P_z^{\mathrm{syn}} \rangle = \frac{7}{16}$, $\langle P_x^{\mathrm{syn}} \rangle = \frac{2}{16}$) and the linear phase $\langle \tilde{P}_j \rangle$ are highlighted with dashed lines. The growth rate Γ_{Bx} of the magnetic field energy is plotted on the right axis (dashed line).

B. Determining the linear phase via the polarization signature

The linear KHI phase can be identified by the polarization of the emitted radiation [Fig. 2]. It starts, when our model $\langle \tilde{P}_j \rangle$ is a better match for the simulated degree of polarization $\langle P_j \rangle$ than a simple synchrotron radiation calculation [31], $\langle P_j^{\mathrm{syn}} \rangle$, approximating randomly quivering electrons during the initial phase. The linear phase ends when the deviations from our model start to grow again. Based on such a selection, the linear phase ranges from $t \approx 9\,\omega_{pe}^{-1}$ to $28\,\omega_{pe}^{-1}$. This definition of the linear KHI regime is in good agreement with a corresponding classification using the B_x-field energy growth rate Γ_{Bx} [Fig. 2], where the FWHM extends from $9\,\omega_{pe}^{-1}$ to $31\,\omega_{pe}^{-1}$.

Comparison of model and simulation results for component-wise degree of polarization [Fig. 2] shows that the temporally and spatially varying injection into the KHI magnetic field of the billions of electrons simulated is well approximated by our model of non-interacting KHI vortex trajectories. The remaining shift in polarization $\langle P_x \rangle > \langle \tilde{P}_x \rangle$ and $\langle P_y \rangle < \langle \tilde{P}_y \rangle$ originates primarily from the spatially non-homogeneous magnetic fields along the y-axis. The stronger acceleration at maximum magnetic field during the upward and downward motion

Table I. Parameters of the KHI large-scale simulation using PIConGPU [14].

computational domain	$480 \times 46 \times 46\,c/\omega_{pe}$
mesh layout (cells)	$8000 \times 768 \times 768$
number of particles per cell	16 (8 for each e^- and p^+)
frequencies	512 from $0.014\omega_{pe}$ to $14\omega_{pe}$
virtual radiation detectors	481 over solid angle $\Omega = \pi$

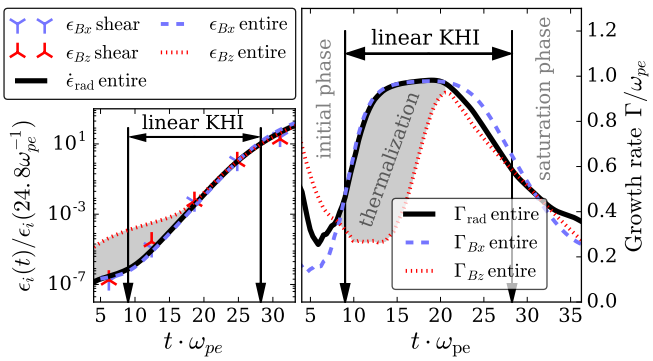

Figure 3. (Left) shows equal temporal evolution between the radiation power $\dot{\epsilon}_{\rm rad}$ from the *entire* stream and the magnetic field energy (ϵ_{Bx},ϵ_{Bz}) on the *shear* surface. The deviation between ϵ_{Bz} from the *entire* plasma and $\dot{\epsilon}_{\rm rad}$ shows that radiation is solely emitted from the KHI. (Right) illustrates the equality of the growth rate $\Gamma_{\rm rad}$ of the radiation power and the growth rate Γ_{Bx} of the *entire* magnetic field energy stored in the B_x component, which best represents the evolution of B_z on the *shear* during the linear phase.

($\boldsymbol{\beta} \parallel \boldsymbol{e}_y$ with $\dot{\beta}_x > \dot{\beta}_y$) of an electron near the shear interface, compared to the turning points ($\boldsymbol{\beta} \parallel \boldsymbol{e}_x$) within the streams at lower magnetic field strength leads to an increased x-polarization $\langle\, P_x \,\rangle > \langle\, \tilde{P}_x \,\rangle = \langle\, \tilde{P}_y \,\rangle > \langle\, P_y \,\rangle$.

C. Determining the KHI growth rate via radiation

The magnetic field energy on the *shear* surface (of both B_z and B_x) and the radiation power $\dot{\epsilon}_{\rm rad}$ from the *entire* plasma show the same temporal evolution during the linear phase [Fig. 3 left]. Comparing this to the component-wise magnetic field energy of the *entire* plasma stream shows that ϵ_{Bx} follows the same evolution, because it is the only magnetic field component driven solely by the KHI, whereas ϵ_{Bz} is initially dominated by thermalization in the bulk of the jet. At the start, the thermalization overshadows the contribution of the KHI and only after $t > 20\omega_{pe}^{-1}$ the exponentially growing B_z in the shear region overcomes the field of the bulk. Since the total energy of B_x of the *entire* plasma evolves equally to B_z on the *shear* surface, we argue that it is a better quantity to compare the results of simulation and model.

In Fig. 3 (right side), we show the time-resolved evolution of the growth rates by computing the logarithmic difference of the discretized simulation results $\Gamma_f(t_k) = \log[f(t_{k+1})/f(t_{k-1})]/(t_{k+1} - t_{k-1})$ with t_k being the $k^{\rm th}$ simulation time step and f being $\langle\, \dot{\epsilon}_{\rm rad} \,\rangle$ or $\epsilon_{B\{x,y,z\}}$ to calculate either $\Gamma_{\rm rad}$ or $\Gamma_{B\{x,y,z\}}$.

The temporal evolution of the radiation power growth rate $\Gamma_{\rm rad}$ of the *entire* simulation [Fig. 3 right] matches that of the magnetic field energy growth rate Γ_{Bx} from the KHI which equals the growth rate of ϵ_{Bz} on the *shear* surface. During the linear phase, Γ_{Bx} follows the radiation growth rate $\Gamma_{\rm rad}$ with a maximum deviation of 11%. After the KHI overcomes the thermalization in the bulk at $t > 20\omega_{pe}^{-1}$, the growth rate Γ_{Bz} of ϵ_{Bz} from the *entire* plasma stream equals $\Gamma_{\rm rad}$, differing by less than 8%. The agreement of $\Gamma_{\rm rad}$ with Γ_{Bx} over the entire linear phase demonstrates that the radiation originates only from the shear surface and is not overshadowed by emission from the bulk: $\Gamma_{\rm rad} = \tilde{\Gamma}_{\rm rad}$. We find the growth rate of the KHI to be $\Gamma = \Gamma_{\rm rad}/2 = 0.48\,\omega_{pe}$.

This shows that our model [Eq. (2)] is a useful approximation - in spite of non-homogeneous fields during the linear phase. The latter is in the dynamics dominated by the exponentially growing magnetic field, which is approximately 5 times stronger than the maximal change in magnetic field due to the the spatial motion of an electron in the interface region.

V. RADIATION PRIOR AND SUBSEQUENT TO THE LINEAR PHASE

The particle-in-cell simulation enables us to further investigate the prior *initial* and subsequent *saturation* regimes of the KHI and show that they emit radiation with very different polarization and thus allow a clear identification of the linear KHI regime by observing these changes in polarization degree [Fig. 2].

Before the onset of the linear KHI regime, the radiation predominantly originates from the thermal jitter motion of the electrons inside the two still self-contained, counter-propagating plasma streams. In general, radiation spectra from jitter motion often differ from synchrotron spectra, deviating in both critical frequency and spectral shape [33]. However, for the sake of simplicity, we approximate the polarization signature of the initial phase by synchrotron radiation $\langle\, P_j^{\rm syn} \,\rangle$ as marked by dashed lines in Fig. 2. They agree with the initial polarization degree observed in the simulation and are clearly distinguishable from the characteristic polarization degree of the linear KHI phase.

In the KHI saturation phase, when the magnetic field at the shear interface becomes strong enough to trap electrons in vortices and thus keep electrons from crossing into the counter-streaming jet, the growth of the magnetic field levels off and stops. At the same time, current sheets surrounding the shear interfaces [15] give rise to strong electric fields normal to the shear layers. Due to this additional acceleration by electric fields, the radiation power growth rate $\Gamma_{\rm rad}$ becomes larger than the magnetic field energy growth rates Γ_{Bx} and Γ_{Bz} [Fig. 3]. Electrons trapped in the vortex reach their peak energy in the middle of the shear layer, where they move normal to the interface and thus radiate primarily into the y-direction. Hence, according to the γ^4-scaling of synchrotron radiation [31], they radiate predominantly with P_x polarization. This leads to an increasing anisotropy between the polarization components $\langle\, P_x \,\rangle \gg \langle\, P_y \,\rangle$ in the saturation phase [Fig. 2]. Similarly, but to a lesser extent, P_z is driven by E_y and B_x, which have grown due to the electron bunching by the transverse KHI [12].

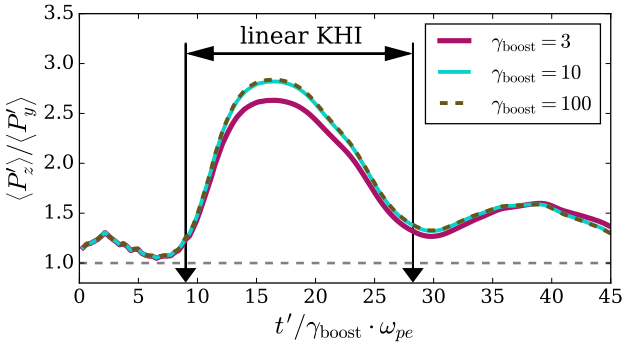

Figure 4. shows the ratio between the polarization $\langle P'_y \rangle$ and $\langle P'_z \rangle$ for several boosts in x-direction with $\gamma_{\rm boost}$ being the respective Lorentz factor. The peaking anisotropy between the polarizations is a hallmark of the KHI linear phase.

VI. IMPLICATION FOR OBSERVATIONS

Until now our results are given in a relative velocity frame. However, astrophysical jets are observed in a very different frame of reference, so that their relativistic motion towards an earth-bound observer leads to Lorentz-boosted radiation emitted in a narrow cone. Since the polarization components $\langle P_j \rangle$ are averaged over ensembles of electrons, time, observation directions and frequencies, they generally do not Lorentz-transform in a trivial manner. Hence the question arises whether it is still possible to identify and characterize KHI in an observer reference frame on earth.

Based on the same data as in Fig. 2, but prior to averaging the results over frequencies and observation directions, we apply a Lorentz-boost in x-direction with Lorentz factor $\gamma_{\rm boost}$ to the electromagnetic field of the emitted radiation [31]. Since $\langle P'_x \rangle$ almost vanishes in the boosted radiation, which is emitted predominantly in x-direction, we use the ratio $\langle P'_z \rangle / \langle P'_y \rangle$ [Fig. 4] as indicator for a transversal polarization anisotropy. The results in Fig. 4 show only a weak dependence with respect to $\gamma_{\rm boost}$, so that this confirms the polarization anisotropy as a hallmark signature of the linear KHI regime.

Thus, after detecting the linear KHI regime in observations and measuring the Lorentz factor $\gamma_{\rm boost}$ of the relativistic boost by an independent diagnostic technique, one can deduce the corresponding instability growth rate by measuring the growth rate $\Gamma'_{\rm rad}$ of total emitted radiation power and rescaling it to compensate time dilation $\Gamma = \Gamma'_{\rm rad}/2 \cdot \gamma_{\rm boost}$. Such a growth rate measurement, due to the large variability in plasma density and Lorentz factors observed in relativistic jets [29, 34, 35], would be in the radio to microwave frequency range and take subseconds to minutes or hours.

Such estimates for temporal scales that need to be resolved in realistic astrophysical observations, as well as in laboratory experiments, take into account the known growth rate scaling of the Kelvin-Helmholtz instability with respect to the relativistic velocity shear γ_e, the density contrast of the respective streams n_1/n_2 and the spatial extent of the shear gradient. First, the growth rate Γ of the mushroom instability decreases according to $\Gamma \sim \beta \cdot \gamma_e^{-1/2} = c_1$ with increasing relative shear velocity [12]. Secondly, a density contrast ($n_1/n_2 \neq 1$) between both streams reduces the growth rate of the KHI further as described in detail in [10]. For the special case of a highly relativistic jet ($\gamma_e \gg 1$) with a density n_1 shearing on an ambient gas with higher density n_2 than the jet: $n_2 \gg n_1/\gamma_e$, the growth rate is reduced by a factor $c_2 = 1/\sqrt{2}$ [12]. Finally, the growth rate is reduced due to a non-steplike velocity shear profile. Following numerical calculations [10], a characteristic shear gradient of more than one plasma skin depth will decrease the growth rate by a factor $c_3 = 0.2$. With decreasing growth rate, the duration of the linear phase and thus the observation time increases inversely $T \sim \Gamma^{-1}$.

For an exemplary astrophysical plasma jet with a Lorentz factor of approximately $\gamma_e = \gamma_{\rm boost} = 100$ and a density around $n_1 = 10^{-4}\,{\rm cm}^{-3}$ shearing on a quasi-stationary ambient gas of density $n_2 \sim 10^{-4} - 10^{-3}\,{\rm cm}^{-3}$ [29], the observed duration of the linear phase is increased due to the aforementioned factors as well as the relativistic time dilatation. Assuming the duration of the linear phase in the relative velocity frame is similar to our simulation $T \approx 19\omega_{pe}^{-1}$, the observed duration is $T' \approx c_1^{-1} \cdot c_2^{-1} \cdot c_3^{-1} \cdot \gamma_{\rm boost} \cdot T > 4\,{\rm min}$. Thus, the characteristic radiation signature can be observed at frequencies higher than the plasma frequency. According to the relativistic Doppler shift $f' \gg \sqrt{\frac{1+\beta_{\rm boost}}{1-\beta_{\rm boost}}} \cdot \frac{\omega_{pe}}{2\pi}$ the radiation would be in the radio frequency range.

In recent laboratory plasma experiments, the KHI was observed at plasma densities around $n_e \sim 10^{17}\,{\rm cm}^{-3}$ [36, 37]. If such a plasma jet reaches[2] $\gamma_{\rm boost} = 17$, the linear phase can be observed for $T' \sim 100\,{\rm ps}$. For such a scenario, the characteristic radiation will be in the near-infrared to optical range.

Since we directly linked the radiation signature to the growth mechanism defining the KHI instability, we can exploit these scaling to extrapolate to realistic astrophysical jets in the sparse interstellar medium or dense laboratory plasmas at ultrafast time scales. Especially, if a specific physics scenario prevents the existence of a KHI and thus a linear regime, there will be no characteristic growth of magnetic fields at a shear layer, thus no polarized-radiation from a shear-layer and vice versa.

VII. SUMMARY

To summarize, we have shown in a large-scale particle-in-cell simulation of the Kelvin-Helmholtz instability that the evolution of polarization of emitted electro-magnetic

[2] This is the respective lab frame of the PIC simulation presented in this paper.

radiation is a useful signature to identify the extent of the linear phase of the KHI. For this selected time period, we demonstrated in our comprehensive ab initio simulation that the equality of growth rates [Eq. (5)] is preserved and that we thus are able to determine the growth rate Γ of the instability by measuring the growth rate Γ'_{rad} of the emitted radiation power.

This ability to identify the KHI among other radiation processes and tie its growth rate to specific growth regimes is a vital step towards a better understanding of astro-physical jets, because observed growth rates in radiation can now be linked to KHI models for constraining jet properties, such as jet-to-ambient density contrasts or velocity gradients [38]. Also, the KHI polarization signature is especially useful for distinguishing it against a radiation background of isotropic polarization. Since the transverse polarization anisotropy allows to determine the orientation of KHI shear interfaces, continuous improvements in observational capabilities [39–41] for spatially resolving the polarization of plasma radiation both along and across astrophysical jets will open the way towards mapping the shear layer geometry and its magnetic fields in complex *jet-within-a-jet* geometries [42].

ACKNOWLEDGMENTS

This research used resources of the Oak Ridge Leadership Computing Facility at the Oak Ridge National Laboratory, which is supported by the Office of Science of the U.S. Department of Energy under Contract No. DE-AC05-00OR22725. `https://www.olcf.ornl.gov/kb_articles/olcf-acknowledgement/`

[1] T. Grismayer, E. P. Alves, R. A. Fonseca, and L. O. Silva, Physical Review Letters **111**, 015005 (2013).
[2] M. Tavani, A. Bulgarelli, G. Piano, S. Sabatini, E. Striani, Y. Evangelista, A. Trois, G. Pooley, S. Trushkin, N. Nizhelskij, *et al.*, Nature **462**, 620 (2009).
[3] M. Punch, C. W. Akerlof, M. Cawley, M. Chantell, D. Fegan, S. Fennell, J. Gaidos, J. Hagan, A. Hillas, Y. Jiang, *et al.*, Nature (1992).
[4] J. Gaidos, C. W. Akerlof, S. Biller, P. Boyle, A. Breslin, J. Buckley, D. Carter-Lewis, M. Catanese, M. Cawley, D. Fegan, *et al.*, Nature (1996).
[5] Y. Uchiyama, C. M. Urry, C. C. Cheung, S. Jester, J. V. Duyne, P. Coppi, R. M. Sambruna, T. Takahashi, F. Tavecchio, and L. Maraschi, The Astrophysical Journal **648**, 910 (2006).
[6] S. Jester, D. Harris, H. L. Marshall, and K. Meisenheimer, The Astrophysical Journal **648**, 900 (2006).
[7] O. A. Hurricane, V. A. Smalyuk, K. Raman, O. Schilling, J. F. Hansen, G. Langstaff, D. Martinez, H.-S. Park, B. A. Remington, H. F. Robey, J. A. Greenough, R. Wallace, C. A. Di Stefano, R. P. Drake, D. Marion, C. M. Krauland, and C. C. Kuranz, Phys. Rev. Lett. **109**, 155004 (2012).
[8] E. P. Alves, T. Grismayer, M. G. Silveirinha, R. A. Fonseca, and L. O. Silva, Plasma Physics and Controlled Fusion **014025**, 14025 (2015), arXiv:1506.08715.
[9] P. Henri, S. Cerri, F. Califano, F. Pegoraro, C. Rossi, M. Faganello, O. Šebek, P. Trávníček, P. Hellinger, J. Frederiksen, *et al.*, Physics of Plasmas **20**, 102118 (2013).
[10] E. Alves, T. Grismayer, R. Fonseca, and L. Silva, New Journal of Physics **16**, 035007 (2014).
[11] K.-I. Nishikawa, P. Hardee, I. Duţan, J. Niemiec, M. Medvedev, Y. Mizuno, A. Meli, H. Sol, B. Zhang, M. Pohl, *et al.*, The Astrophysical Journal **793**, 60 (2014).
[12] E. P. Alves, T. Grismayer, R. A. Fonseca, and L. O. Silva, Physical Review E **92**, 021101 (2015).
[13] K.-I. Nishikawa, J. Niemiec, M. Medvedev, B. Zhang, P. Hardee, A. Nordlund, J. Frederiksen, Y. Mizuno, H. Sol, M. Pohl, D. Hartmann, M. Oka, and G. Fishman, Advances in Space Research **47**, 1434 (2011), Neutron Stars and Gamma Ray Bursts.
[14] M. Bussmann, H. Burau, T. E. Cowan, A. Debus, A. Huebl, G. Juckeland, T. Kluge, W. E. Nagel, R. Pausch, F. Schmitt, *et al.*, in *Proceedings of the International Conference on High Performance Computing, Networking, Storage and Analysis*, SC '13 (ACM, New York, NY, USA, 2013) pp. 5:1–5:12.
[15] E. P. Alves, T. Grismayer, S. F. Martins, F. Fiza, R. A. Fonseca, and L. O. Silva, The Astrophysical Journal Letters **746**, L14 (2012).
[16] S. Kiselev, A. Pukhov, and I. Kostyukov, Phys. Rev. Lett. **93**, 135004 (2004).
[17] C. B. Hededal and Å. Nordlund, arXiv preprint astro-ph/0511662 (2005).
[18] A. G. Khachatryan, F. A. van Goor, and K. J. Boller, , 14 (2008), arXiv:0805.0948.
[19] J. Martins, S. Martins, R. Fonseca, and L. Silva, in *SPIE Europe Optics+ Optoelectronics* (International Society for Optics and Photonics, 2009) pp. 73590V–73590V.
[20] L. Sironi and A. Spitkovsky, The Astrophysical Journal Letters **707**, L92 (2009).
[21] K.-I. Nishikawa, M. Medvedev, B. Zhang, P. Hardee, J. Niemiec, Å. Nordlund, J. Frederiksen, Y. Mizuno, H. Sol, and G. J. Fishman, in *American Institute of Physics Conference Series*, American Institute of Physics Conference Series, Vol. 1133, edited by C. Meegan, C. Kouveliotou, and N. Gehrels (2009) pp. 235–237, arXiv:0901.4058 [astro-ph.HE].
[22] S. G. Rykovanov, M. Chen, C. G. R. Geddes, C. B. Schroeder, E. Esarey, and W. P. Leemans, AIP Conference Proceedings **1507**, 399 (2012).
[23] T. Haugbølle, J. T. Frederiksen, and Å. Nordlund, Physics of Plasmas **20** (2013), 10.1063/1.4811384, arXiv:arXiv:1211.4575v3.
[24] K.-I. Nishikawa, P. Hardee, Y. Mizuno, I. Duţan, B. Zhang, M. Medvedev, E. Choi, K. Min, J. Niemiec, Å. Nordlund, *et al.*, *EPJ Web of Conferences*, **61**, 02003 (2013).
[25] K.-I. Nishikawa, P. Hardee, I. Dutan, B. Zhang, A. Meli, E. Choi, K. Min, J. Niemiec, Y. Mizuno, M. Medvedev,

et al., arXiv:1412.7064 (2014).
[26] J. Martins, M. Vranic, T. Grismayer, J. Vieira, R. Fonseca, and L. Silva, Plasma Physics and Controlled Fusion **58**, 014035 (2015).
[27] R. Pausch, A. Debus, R. Widera, K. Steiniger, A. Huebl, H. Burau, M. Bussmann, and U. Schramm, Nucl. Instrum. Meth. A. **740**, 250 (2014), Proc. of 1st EAAC Workshop 2013.
[28] R. Pausch, H. Burau, M. Bussmann, J. Couperus, T. Cowan, A. Debus, A. Huebl, A. Irman, A. Köhler, U. Schramm, *et al.*, *Proceedings of IPAC2014*, , MOPRI069 (2014).
[29] A. Ferrari, Annual Review of Astronomy and Astrophysics **36**, 539 (1998).
[30] W. Zhang, A. MacFadyen, and P. Wang, The Astrophysical Journal Letters **692**, L40 (2009).
[31] J. D. Jackson, *Classical Electrodynamics*, 3rd ed. (John Wiley and Sons, Inc., 1999) Chap. 14.6.
[32] H. Burau, R. Widera, W. Hönig, G. Juckeland, A. Debus, T. Kluge, U. Schramm, T. E. Cowan, R. Sauerbrey, and M. Bussmann, Plasma Science, IEEE Transactions on **38**, 2831 (2010).
[33] M. V. Medvedev, The Astrophysical Journal **540**, 704 (2000), 0001314v2.
[34] J.-M. Martí, in *ASP Conference Series*, Vol. 386, edited by T. A. Rector and D. S. De Young (2008) pp. 417–428.
[35] P. E. Hardee, in *EPJ Web of Conferences*, Vol. 61 (EDP Sciences, 2013) p. 02001.
[36] Y. Kuramitsu, Y. Sakawa, S. Dono, C. D. Gregory, S. A. Pikuz, B. Loupias, M. Koenig, J. N. Waugh, N. Woolsey, T. Morita, T. Moritaka, T. Sano, Y. Matsumoto, A. Mizuta, N. Ohnishi, and H. Takabe, Phys. Rev. Lett. **108**, 195004 (2012).
[37] J. Meinecke, P. Tzeferacos, A. Bell, R. Bingham, R. Clarke, E. Churazov, R. Crowston, H. Doyle, R. P. Drake, R. Heathcote, M. Koenig, Y. Kuramitsu, C. Kuranz, D. Lee, M. MacDonald, C. Murphy, M. Notley, H.-S. Park, A. Pelka, A. Ravasio, B. Reville, Y. Sakawa, W. Wan, N. Woolsey, R. Yurchak, F. Miniati, A. Schekochihin, D. Lamb, and G. Gregori, Pnas **112**, 1502079112 (2015), arXiv:arXiv:1408.1149.
[38] S. Massaglia, in *Jets in Young Stellar Objects*, Vol. 287 (Springer Netherlands, Dordrecht, 2003) pp. 223–233.
[39] K. Hada, A. Doi, M. Kino, H. Nagai, Y. Hagiwara, and N. Kawaguchi, Nature **477**, 185 (2011).
[40] R. B. Wayth, W. F. Brisken, A. T. Deller, W. A. Majid, D. R. Thompson, S. J. Tingay, and K. L. Wagstaff, The Astrophysical Journal **735**, 97 (2011).
[41] T. P. Krichbaum, A. Roy, R.-S. Lu, J. A. Zensus, V. Fish, S. Doeleman, and Event Horizon Telescope (EHT) Collaboration, Proceedings of the 12th European VLBI Network Symposium and Users Meeting (EVN 2014). 7-10 October 2014. Cagliari , 7 (2014).
[42] T. Piran, Reviews of Modern Physics **76**, 1143 (2005).